Helicity conservation by flow across scales in reconnecting vortex links and knots

Martin W. Scheeler[a,1,2], Dustin Kleckner[a,1,2], Davide Proment[b], Gordon L. Kindlmann[c], and William T. M. Irvine[a,2]

[a]James Franck Institute, Department of Physics, and [c]Computation Institute, Department of Computer Science, The University of Chicago, Chicago, IL 60637; and [b]School of Mathematics, University of East Anglia, Norwich Research Park, Norwich NR4 7TJ, United Kingdom

Edited* by Leo P. Kadanoff, The University of Chicago, Chicago, IL, and approved August 28, 2014 (received for review April 19, 2014)

The conjecture that helicity (or knottedness) is a fundamental conserved quantity has a rich history in fluid mechanics, but the nature of this conservation in the presence of dissipation has proven difficult to resolve. Making use of recent advances, we create vortex knots and links in viscous fluids and simulated superfluids and track their geometry through topology-changing reconnections. We find that the reassociation of vortex lines through a reconnection enables the transfer of helicity from links and knots to helical coils. This process is remarkably efficient, owing to the antiparallel orientation spontaneously adopted by the reconnecting vortices. Using a new method for quantifying the spatial helicity spectrum, we find that the reconnection process can be viewed as transferring helicity between scales, rather than dissipating it. We also infer the presence of geometric deformations that convert helical coils into even smaller scale twist, where it may ultimately be dissipated. Our results suggest that helicity conservation plays an important role in fluids and related fields, even in the presence of dissipation.

helicity | fluid topology | vortex reconnections | superfluid vortices | topological fields

In addition to energy, momentum, and angular momentum, ideal (Euler) fluids have an additional conserved quantity—helicity (Eq. **1**)—which measures the linking and knotting of the vortex lines composing a flow (1). For an ideal fluid, the conservation of helicity is a direct consequence of the Helmholtz laws of vortex motion, which both forbid vortex lines from ever crossing and preserve the flux of vorticity, making it impossible for linked or knotted vortices to ever untie (1, 2). Because conservation laws are of fundamental importance in understanding flows, the question of whether this topological conservation law extends to real, dissipative systems is of clear and considerable interest. The general importance of this question is further underscored by the recent and growing impact knots and links are having across a range of fields, including plasmas (3, 4), liquid crystals (5, 6), optical (7), electromagnetic (8), and biological structures (9–11), cosmic strings (12, 13), and beyond (14). Determining whether and how helicity is conserved in the presence of dissipation is therefore paramount in understanding the fundamental dynamics of real fluids and the connections between tangled fields across systems.

The robustness of helicity conservation in real fluids is unclear because dissipation allows the topology of field lines to change. For example, in viscous flows vorticity will diffuse, allowing nearby vortex tubes to "reconnect" (Fig. 1 *A*–*C*), creating or destroying the topological linking of vortices. This behavior is not unique to classical fluids: analogous reconnection events have also been experimentally observed in superfluids (15) and coronal loops of plasma on the surface of the sun (16). In general, these observed reconnection events exhibit divergent, nonlinear dynamics that makes it difficult to resolve helicity dynamics theoretically (4, 17, 18). On the other hand, experimental tests of helicity conservation have been hindered by the lack of techniques to create vortices with topological structure. Thanks to a recent advance (19), this is finally possible.

By performing experiments on linked and knotted vortices in water, as well as numerical simulations of Bose–Einstein condensates [a compressible superfluid (20)] and Biot–Savart vortex evolution, we investigate the conservation of helicity, in so far as it can be inferred from the center-lines of reconnecting vortex tubes. We describe a new method for quantifying the storage of helicity on different spatial scales of a thin-core vortex: a "helistogram." Using this analysis technique, we find a rich structure in the flow of helicity, in which geometric deformations and vortex reconnections transport helicity between scales. Remarkably, we find that helicity can be conserved even when vortex topology changes dramatically, and identify a system-independent geometric mechanism for efficiently converting helicity from links and knots into helical coils.

Topology and Helicity

Topology in a fluid is stored in the linking of vortex lines. The simplest example of linked vortex lines is a joined pair of rings (Fig. 1*A*); however, the same topology can be obtained with very different geometries, for example, by twisting or coiling a pair of rings (Fig. 1 *D* and *E*).

Vortex loops in fluids (e.g., Fig. 1 *B* and *C*) consist of a core region of concentrated vorticity, $\boldsymbol{\omega}$, that rotates around the vortex center-line, surrounded by irrotational fluid motion. In the language of vortex lines, vortices should therefore be regarded as "bundles" of vortex "filaments" (e.g., Fig. 1 *F* and *G*), more akin to stranded rope than an infinitesimal line. In this

Significance

Ideal fluids have a conserved quantity—helicity—which measures the degree to which a fluid flow is knotted and tangled. In real fluids (even superfluids), vortex reconnection events disentangle linked and knotted vortices, jeopardizing helicity conservation. By generating vortex trefoil knots and linked rings in water and simulated superfluids, we observe that helicity is remarkably conserved despite reconnections: vortex knots untie and links disconnect, but in the process they create helix-like coils with the same total helicity. This result establishes helicity as a fundamental building block, like energy or momentum, for understanding the behavior of complex knotted structures in physical fields, including plasmas, superfluids, and turbulent flows.

Author contributions: M.W.S., D.K., and W.T.M.I. designed research; M.W.S., D.K., and W.T.M.I. performed research; M.W.S., D.K., D.P., and G.L.K. contributed new reagents/analytic tools; M.W.S., D.K., G.L.K., and W.T.M.I. analyzed data; and M.W.S., D.K., and W.T.M.I. wrote the paper.

Conflict of interest statement: The research groups of W.T.M.I. and L.P.K. both receive funding from The University of Chicago Materials Research and Engineering Centers grant (supported by the National Science Foundation). This grant supports a large number of researchers, and there is no collaboration between W.T.M.I. and L.P.K. on this or any other project.

*This Direct Submission article had a prearranged editor.

[1]M.W.S. and D.K. contributed equally to this work.

[2]To whom correspondence may be addressed. Email: scheeler@uchicago.edu, dkleckner@uchicago.edu, or wtmirvine@uchicago.edu.

This article contains supporting information online at www.pnas.org/lookup/suppl/doi:10.1073/pnas.1407232111/-/DCSupplemental.

case, topology can be stored either by linking and knotting of bundles, or by linking of nearby filaments within a single bundle.

The hydrodynamic helicity quantifies the degree of vortex linking present in a flow; in terms of the flow field, $\boldsymbol{u}(\boldsymbol{r})$ (where $\boldsymbol{r}$ is the spatial coordinate), it is given by the following:

$$\mathcal{H} = \int \boldsymbol{u} \cdot \boldsymbol{\omega} \, d^3 r, \qquad [1]$$

where the vorticity is $\boldsymbol{\omega} = \nabla \times \boldsymbol{u}$. This quantity is exactly conserved for ideal fluids (1, 21). The connection between helicity and the linking between vortex tubes was first noted by Moffatt (1), who showed that for a flow consisting of thin, closed vortex lines $\mathcal{C}_n$, the helicity is equivalently given by the following:

$$\mathcal{H} = \sum_{i,j} \Gamma_i \Gamma_j \frac{1}{4\pi} \oint_{\mathcal{C}_i} \oint_{\mathcal{C}_j} \frac{\boldsymbol{x}_i - \boldsymbol{x}_j}{|\boldsymbol{x}_i - \boldsymbol{x}_j|^3} \cdot (d\boldsymbol{\ell}_i \times d\boldsymbol{\ell}_j), \qquad [2]$$

where Γ_i and $\boldsymbol{x}_i$ correspond to the circulation (vorticity flux) and path of vortex tube $\mathcal{C}_i$. The resulting double path integral was recognized as the Gauss linking integral, which measures the linking between the paths $\mathcal{C}_i$ and $\mathcal{C}_j$ or in the case $i = j$ the writhe (coiling and knotting) of a single path.

For finite thickness vortex tubes, one may subdivide the bundle into N infinitesimal filaments each with strength Γ/N, and compute Eq. **2** in the limit $N \to \infty$ (22, 23). The result is conveniently expressed as the sum of three terms, each geometrically distinct contributions to the same measure of topology:

$$\mathcal{H} = \sum_{i \neq j} \Gamma_i \Gamma_j \, \mathcal{L}_{ij} + \sum_i \Gamma_i^2 \, (Wr_i + Tw_i), \qquad [3]$$

where $\mathcal{L}_{ij}$ is the linking number between bundles i and j, Wr_i is the writhe of the bundle center-line, and Tw_i is the total twist of each bundle. Both the linking number and writhe are given by the Gauss linking integral for the bundle center-line. The writhe of a curve quantifies its total helix-like coiling and knotting. The twist is given by $Tw = \frac{1}{2\pi} \oint (\hat{\boldsymbol{n}} \times \partial_s \hat{\boldsymbol{n}}) \cdot d\boldsymbol{\ell}$, where $\hat{\boldsymbol{n}}$ is a normal vector on each path that describes the bundle orientation.

The first sum of Eq. **3**, for $i \neq j$, measures the linking between bundles, whereas the second sum, over i, measures the linking between filaments within each bundle. The topological contribution of twist can be visualized by subdividing a ring (with flux Γ) into a pair of filaments (with flux $\Gamma/2$), that twist around each other as shown in Fig. 1*D*. Similarly, the topological contribution of writhe can be seen in Fig. 1*E*; in each case, the resulting helicity is $\mathcal{H} = 1\Gamma^2$. Each of these examples produces a helicity equal to an integer multiple of Γ^2; however, for a bundle, the helicity is a flux-weighted average linking, which need not be an integer multiple of Γ^2 (e.g., if a filament does not close in a single trip around the bundle) (23). The bundle sections shown in Fig. 1 *F* and *G* each have a helicity of $\mathcal{H} \sim 0.7\Gamma^2$, resulting from twist or coil, respectively. The topological equivalence of these two geometrically distinct bundles can be seen by taking the coiled bundle and pulling on the ends; straightening out the coil results in a compensating twist, which conserves the helicity.

Although the linking number between bundles and the writhe of each bundle can be calculated from the center-line alone, measuring the twist requires additional information about the fine structure of the vortex core, which is challenging to resolve experimentally. For the remainder of the paper, we consider only the "center-line helicity," given by the following:

$$\mathcal{H}_c / \Gamma^2 = \sum_{i \neq j} \mathcal{L}_{ij} + \sum_i Wr_i. \qquad [4]$$

This geometric quantity is equivalent to the total helicity if we assume that all vortex tubes have the same circulation, $\Gamma_i \to \Gamma$, and are locally untwisted, $Tw_i = 0$ (see *SI Text, Definition of the Center-Line Helicity* and Fig. S1 for a discussion of the definition of center-line helicity). We note that twist is naturally dissipated by viscosity, and for a twisted straight line vortex filament, this occurs at a rate $\frac{\partial_t Tw}{Tw} = -\frac{8\pi\nu}{A_{\text{eff}}}$, where ν is the kinematic viscosity and A_{eff} is the bundle cross sectional area (*SI Text, Helicity Dissipation for a Twisted Core*). For typical experimental parameters, this can be estimated to be faster than the overall dynamics of the center-line motion.

Methods

To explore the behavior of thin-core vortices in experiment, we create shaped vortex loops in water, akin to the familiar smoke ring, but imaged with buoyant microbubbles instead of smoke. Our vortex loops are generated by impulsively accelerating specially shaped, 3D printed hydrofoils (see Fig. S2 for corresponding meshes and hydrofoil profile). Upon acceleration, a "starting vortex" whose shape traces the trailing edge of the hydrofoil is shed and subsequently evolves under its own influence; using this technique, it is possible to generate arbitrary geometry and topology, including links and knots (19). To study the effects of topology, we focus on the behavior of the most elemental linked and knotted vortices: Hopf links and trefoil knots, both of which can be created with high fidelity. Our vortices have a typical width of 150 mm and circulation of $\Gamma = 20{,}000$ mm^2/s, and we use water as the experimental fluid. The Reynolds number is of order $Re \sim 2 \times 10^4$.

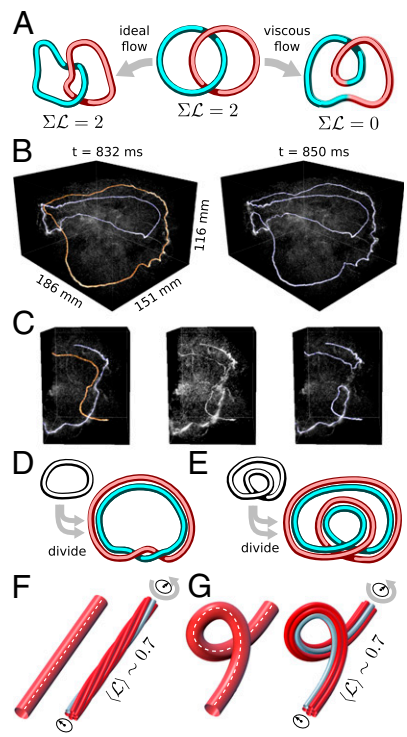

Fig. 1. (*A*) A sketch of the evolution of vortex tube topology in ideal (Euler) and viscous (Navier–Stokes) flow. Dissipative flows allow for reconnections of vortex tubes, and so tube topology is not conserved. (*B*) Two frames of a 3D reconstruction of a vortex reconnection in experiment, which turns an initially linked pair of rings into a single twisted ring. (*C*) A close-up view of the reconnection in *B*. (*D*) If a tube is subdivided into multiple tubes, linking between the two may be created by introducing a twist into the pair. (*E*) Similarly, if a coiled tube is subdivided, linking can result even without adding twist. This can be seen either by calculating the linking number for the pair, or imagining trying to separate the two. (*F*) In a continuum fluid, the vortex tube may be regarded as a bundle of vortex filaments, which may be twisted. In this case, a twist of $\Delta\theta \sim 0.7 \times 2\pi$ results in a total helicity of $\mathcal{H} \sim 0.7\Gamma^2$. (*G*) If the vortex tube is coiled, linking will also be introduced, as in *E*. Conceptually, this coiling can be regarded as producing a net rotation of the vortex bundle even when it is everywhere locally untwisted.

PHYSICS

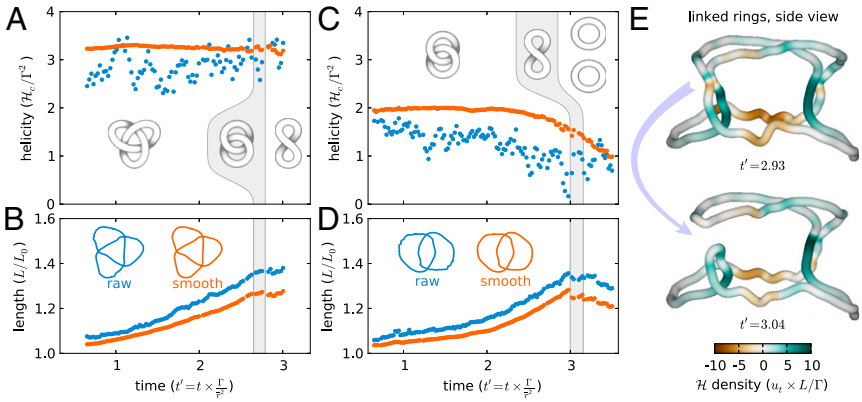

Fig. 2. (*A* and *B*) The computed center-line helicity ($\mathcal{H}_c$) and length for of an experimental trefoil knot vortex through the first two reconnection events (out of three total). The teal data indicate the raw experimental traces, whereas the orange data have been smoothed with a windowed sinc function whose spatial cutoff is $\lambda = 50$ mm (the total vortex length is ~1 m). The gray *Inset* diagrams indicate the topologies at different stages of the vortex evolution. (*C* and *D*) The center-line helicity and length for a linked pair of vortex rings in experiment, through two reconnections. (*E*) Two traces of a pair of initially linked vortices in experiment, just before and after a reconnection event. The traces are colored according to the computed local helicity density, $h = \Gamma u_t$, calculated using the Biot–Savart law.

These vortices are tracked using ~100-μm microbubbles, generated by hydrolysis, which are trapped in the core of the rapidly spinning vortices (e.g., Fig. 1 *B* and *C*). These bubbles are in turn imaged with high-speed laser scanning tomography of a 230×230×230-mm volume at a resolution of 384^3 and a rate of 170 s^{-1}. Using these data, we trace the vortex cores by first identifying line-like features in the volumetric data and then connecting them to create closed 3D paths (24–26), approximated as polygons with ~3,000 points. Some disruption of the imaging and tracking results from vortex reconnections, but careful adjustment of the experimental parameters allows vortices to be tracked immediately before and after reconnections. From these paths, physical quantities such as energy, momentum, and helicity can be directly calculated as path integrals, and the geometric nature of this description allows direct comparison with other fluid systems, including simulations of superfluids and idealized thin core vortex models, both of which will be described later. We rescale all of the vortex lengths in terms of the initial length, L_0, and rescale the time in terms of the inital r.m.s. vortex radius, $\bar{r} = \sqrt{\langle|\boldsymbol{x}|^2\rangle - |\langle\boldsymbol{x}\rangle|^2}$, and circulation, Γ: $t' = t\times\Gamma/\bar{r}^2$ (both $\bar{r}$ and L_0 are calculated from the designed vortex geometry, determined by the hydrofoil shape). Technical details for all systems are described in *SI Text, Experimental Vortex Generation* and follow established methods (19, 27–29). Note that, for our experimental vortices, we can estimate the rate of twist dissipation as $\partial_t Tw/Tw \sim 5$ s^{-1}, whereas the overall vortex motion has a timescale of order 1 s (*SI Text, Helicity Dissipation for a Twisted Core*).

Experimental Results

As was found in previous studies (18, 19, 27), our initially linked and knotted vortices disentangle themselves through local reconnections into topological trivial vortex rings. This change in tube topology might be expected to result in a corresponding change of the helicity, because it is a global measure of the vortex topology. For example, a reconnection event that changes a pair of linked rings into a single coiled ring (e.g., Fig. 1*A*) should result in a sudden, discontinuous jump of the helicity by $|\Delta\mathcal{H}_c| \sim 1\Gamma^2$. Recently, more detailed analytical results have also indicated that helicity may be dissipated in a reconnection event (17). Remarkably, our experimental measurements of the total center-line helicity, $\mathcal{H}_c$, show that it is nearly unaffected by reconnections (Fig. 2 *A* and *C*). As numerical computation of writhe is sensitive to small-scale noise in the extracted path, applying a small amount of local smoothing to the raw path data dramatically improves the measurement. We do this by convolving the raw vortex center-line traces, $\boldsymbol{x}_i(s)$ (where s is the path-length coordinate), with a windowed sinc function with a spatial cutoff of $\lambda = 50$ mm, which is about 5% of the total vortex length of both the links and knots. Remarkably, we find that a vortex initially shaped into a trefoil vortex knot (Fig. 2 *A* and *B*) is observed to have nearly constant center-line helicity, $\mathcal{H}_c/\Gamma^2 = 3.25 \pm 0.04$, even though it is undergoing dramatic changes in geometry and topology. Similarly, the initially linked pair of rings (Fig. 2 *C* and *D*) also shows no jump in the helicity through reconnection events, even though on longer timescales the center-line helicity is seen to change from $\mathcal{H}_c \sim 2\Gamma^2$ to $\sim 1\Gamma^2$, apparently via geometric deformations. Taken together, we conclude that any jump in helicity is less than $\Delta\mathcal{H}_c \lesssim 0.05\Gamma^2$ per reconnection for our vortices.

The apparent absence of a helicity jump indicates that the vortices are spontaneously arranging themselves into a geometry that allows center-line helicity to be conserved through reconnections. This proceeds via a simple geometric mechanism: at the moment of topology-changing reconnection, the reassociation of vortex lines creates writhing coils in regions that were previously free of writhe, thus converting center-line helicity from linking to writhe (or vice versa) each time a reconnection takes place. The remarkable efficiency of the helicity transfer results from the precise way in which the curves approach each other. The vortex sections where the reconnection is taking place are almost perfectly antiparallel just before the reconnection event (Fig. 1*C*). This means that the reassociation of vortex tubes that occurs during the reconnection will not change the crossing number in any projection of the vortex tube center-line. Because the writhe can be computed as the average crossing number over all orientations, this implies the total linking and writhing, $\sum Lk + \sum Wr$, should be conserved, and hence the center-line helicity as well. (See *SI Text, Theory of Helicity Conservation Through a Reconnection*, and Fig. S3 for a description of this mechanism purely in terms of planar link diagrams.) Alternatively, one can consider the helicity density in the reconnecting region, obtained by computing the tangential flow, $h = \Gamma u_t$ (Fig. 2*E*). If the annihilated sections are close and antiparallel, the sum of this helicity density should approach zero, conserving helicity (1). Interestingly, this antiparallel configuration is expected to form naturally if the vortex tubes are stretching themselves while conserving energy, which seems to happen spontaneously for vortices whose tube topology is nontrivial (19).

Conversion of Linking and Knotting to Coiling on Different Scales. The simple geometric mechanism we find for the conservation of center-line helicity through reconnections implies a transfer of helicity across scales that should be quantifiable. Although volumetric Fourier components have been used as measures of helicity content on different scales for flows with distributed vorticity (30), for thin core vortices the distance along the vortex provides a natural length scale. To quantify the storage of helicity as a function of scale along the vortex filament, we compute the helicity as a function of smoothing, $\mathcal{H}_c(\lambda)$, where λ is a hard spatial cutoff scale introduced by convolving the vortex path with a sinc kernel of variable width (this is the same procedure used to smooth the raw data, described above, but with varying cutoff). When this smoothing is applied, helix-like distortions of the path with period less than λ will be removed, and so the contribution of those helical coils to the overall helicity is also removed. The derivative of this function, $\partial\mathcal{H}_c|_\lambda$, then quantifies the helicity content stored at spatial scale λ (Fig. 3 and Movies S1 and S2).

Ultimately, there is a component of the helicity that is not removed by even long-scale smoothing; for the relatively simple topologies studied here, the resulting writhe is nearly integer.

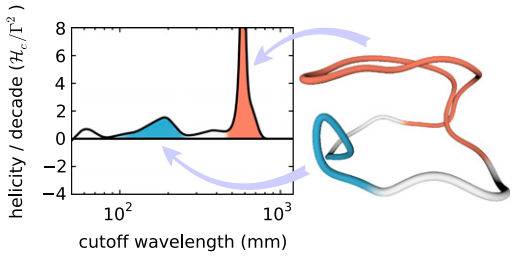

Fig. 3. The coiling component of a helistogram for an experimental pair of linked rings just after the first reconnection ($t' = 3.25$), with a colored image of the experimental data trace used to compute the helistogram. The peaks in the helistogram correspond to coils at two different length scales, which are color coded. In each case, the length of the segment colored is equal to the cutoff wavelength for that peak. Each coil contains approximately one unit of helicity.

This integer component arises because as it is smoothed, the path becomes nearly planar and the integer contribution corresponds to the crossing number in this effective planar projection. We refer to this as an effective integer knotting number, akin to linking, and the component removed by smoothing as "coiling," which is produced by helical distortions.

Fig. 4 shows the helistogram for our trefoil knots and linked rings before, during, and after the reconnection process (see also Movie S3). In both cases, we observe that the initial deformation accompanying the stretching produces small helical deformations across a range of scales; in the case of the trefoil knot, these are nearly perfectly balanced, whereas the linked rings create a strong helix at a scale of 20–30 mm with a helicity opposed to the overall linking. During the reconnections, we see an immediate transfer from knotting or linking to coiling. In the case of the linked rings, the first reconnection creates an unlinked geometry immediately (Fig. 4*B*; $t' = 3.25$), but in doing so creates a large-scale folded coil with a spatial scale of ∼600 mm, which then quickly reconnects to form coils at 100–200 mm (Fig. 3). The trefoil knot (Fig. 4*A* and Movie S4) has similar dynamics; although it is still topologically nontrivial after the first reconnection (Fig. 4*A*; $t' = 2.98$), it becomes a pair of linked rings that unlinks in a similar manner to the initially linked rings.

In both cases, we find that helicity stored on long spatial scales, whether they be knots or links, appears to be intrinsically unstable, cascading through reconnections to smaller spatial scales. Moreover, this process coincides with the overall stretching that occurs when the topology is nontrivial; after the reconnections take place, the length of the vortices appears to stabilize.

Related mechanisms for helicity conservation through reconnections have been suggested in simple models of dissipative plasmas, for example by converting linking to internal twist (22, 31, 32).

Helicity Conservation in Simulated Superfluids. The mechanism we observe for helicity conservation through reconnections is entirely geometric, suggesting it may be present in other fluid-like systems as well. To test this possibility, we simulate the evolution of vortex knots in a superfluid with the Gross–Pitaevskii equation (GPE) (20). Although superfluids are inviscid, they are not ideal Euler fluids; thus, vortex reconnections are possible and vortex topology is not conserved. Unlike a classical fluid, which has finite vortex cores, superfluid vortices are confined to a line-like phase defect (33, 34); here, we track the center-line helicity (Eq. **4**) computed for the phase defect path.

Recently, methods have been demonstrated for creating vortex knots in superfluid simulations (27). We have extended this technique to create initial states with phase defects of arbitrary geometry using velocity integration for flow fields generated by the Biot–Savart law (see *SI Text, Gross-Pitaevskii Equation* for details), allowing us to generate vortices with the same initial shape as our experiments. We simulate the subsequent vortex evolution using standard split-step methods, and extract the vortex shape by tracing the phase defects in the resulting wave function. We model vortices with initial radii of $\bar{r} = 6$–48ξ, where ξ is the healing length that sets the size of a density-depleted region that surrounds the vortex line. (Our simulations use a uniform grid size of 0.5ξ and range in resolution from 64^3 to 512^3.)

As has been previously observed, we find that vortex knots are intrinsically unstable in superfluids, undergoing a topological and geometrical evolution qualitatively similar to our experimental data (Fig. 5; see Fig. S4 and Movie S5 for a corresponding helistogram). In particular, we find that the reconnections are heralded by an overall stretching of the vortex, which abruptly stops after the reconnections take place. Unlike the experimental data, we also observe a discrete jump in the center-line helicity across the reconnection, ranging from $\Delta\mathcal{H}_c \sim 0.1$–$1\Gamma^2$ per reconnection, which is a strong function of the initial vortex size (note that, in the simulations, all three reconnections happen simultaneously). If we compute the helicity jump just across the reconnection event, defined as the time during which the colliding vortices are less than 2ξ apart (i.e., when the density depleted regions have already merged), we find a clear $\Delta\mathcal{H}_c \sim \bar{r}^{-1.0}$ trend. We observe slightly different results when considering the overall drop in helicity across the entire simulation, from $t' = 0$–4, consistent with $\Delta\mathcal{H}_c \sim \bar{r}^{-0.7}$ trend, which may be a combination of prereconnection deformation effects and the reconnection jump. In particular, the prereconnection helicity

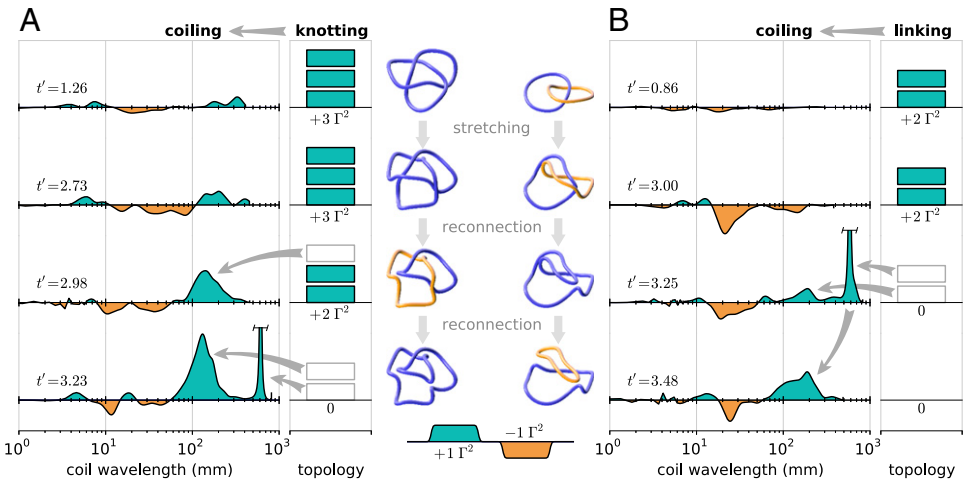

Fig. 4. (*A* and *B*) Helistograms for *A*, a trefoil knot *B*, linked rings in a viscous fluid experiment (the dataset is the same as shown in Fig. 2 *A–D*; the total vortex length is ∼1 m for both). The left portion of each series of plots shows the helicity contribution due to coiling on different spatial scales, obtained by computing $\partial_n\mathcal{H}_c(\lambda = 10^n)$, where λ is the cutoff wavelength for a windowed sinc smoothing. The right portion of each plot shows the irreducible contribution to the helicity originating from the global vortex topology. Both the coiling and topological contributions are scaled so that the total helicity is proportional to the filled area of the plots. The center column shows images of the numerically traced vortices smoothed to $\lambda = 100$ mm.

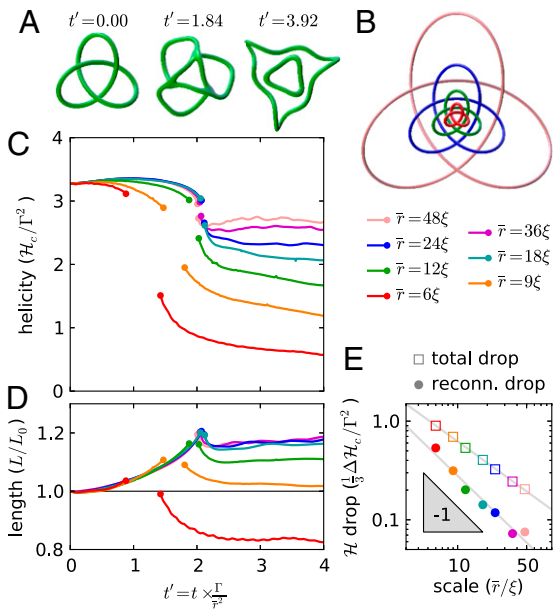

Fig. 5. (*A*) Renderings of density isosurfaces ($\rho=0.5\rho_0$) for a trefoil vortex knot ($\bar{r}=12\xi$), simulated with the GPE. The initially knotted configuration changes to a pair of unlinked rings whose writhe conserves most of the original helicity. (*B*) Renderings of different sized trefoil knots, where the tube radius is given by the healing length, ξ, which acts as an effective core size for the superfluid vortex. (*C* and *D*) The computed center-line helicity ($\mathcal{H}_c$) and length for of a range of GPE-simulated trefoil knots. The data are only shown when the distance between vortex lines is $r_{min}>2\xi$. (*E*) The helicity jump per reconnection event as a function of size ratio for GPE-simulated trefoil knots. The open squares are the total drop between $t'=0$ and $t'=4$, whereas the circles indicate the drop during the reconnection event, defined as the missing region in *C* where the vortex tubes overlap. Larger knots, relative to ξ, are found to conserve helicity better by either measure.

data seems to converge for $\bar{r}\gtrsim 18\xi$, suggesting the finite-core size is not important in this regime before the reconnection.

We attribute the loss of center-line helicity to the fact that the finite size of the depleted density core in the GPE simulations leads the reconnections to begin before the vortices are perfectly antiparallel, resulting in less efficient conservation. It is unclear whether the same effect is present in the experiments, due to the difficulties associated with accurately tracking significantly smaller vortices; however, we note that the expected core-to-vortex size ratio for our experiments is close to that of the largest GPE simulations and we do not observe such a jump. Previous studies of the simulated dynamics of reconnections in superfluids and classical fluids suggest that there may be differences in the details of the reconnection behavior (35–37). Nonetheless, we observe that the same conversion of linking and knotting to coiling is present in our superfluid model, indicating that the geometric mechanism for helicity transport across scales that we find in experiment is generic.

Writhe to Twist Conversion. Although helicity change is usually understood as being associated with topological changes, we also observe a gradual change in center-line helicity even when reconnections are not taking place, for example in the experimental linked rings (Fig. 2*C*) or the GPE simulations before a reconnection (Fig. 5*C*). Because the center-line topology is not changing, this helicity change must be attributable to a geometric effect: coiling must have been dissipated or converted to internal twist, which we do not resolve (or is not present, in the case of the GPE).

A dramatic example of this effect can be seen in "leap-frogging" vortices, where a pair of same-sized vortices placed front to back repeatedly passes through one another. Although this configuration has no center-line helicity if both vortices are perfect rings, a helical winding can be added to one of the rings to give the structure nonzero writhe and hence nonzero center-line helicity. We model the time evolution of this structure as a thin-core vortex using a simple inviscid Biot–Savart model (see *SI Text, Biot-Savart Evolution of Thin Core Vortices* for details), and find that the helicity varies widely as the vortices repeatedly pass through one another (Fig. 6 *E* and *F* and Movie S6).

This variation of the helicity is caused by the fact that the vortices are stretching and compressing each other as a function of time: whenever one vortex passes through another, it must be shrunk to fit inside, resulting in a change of the helix pitch. A simple model of this change can be constructed by first noting that the writhe of a straight helical section is as follows: $Wr_{\text{helix}}=N(1-\cos\theta)$, where N is the number of turns and θ is the pitch angle. In the limit of a small pitch angle: $Wr_{\text{helix}}\approx\frac{2\pi^2a^2}{L^2}N^3$, where a and L are the radius and length of the cylinder around which the helix is wound (Fig. 6*D* and *SI Text, Definition of*

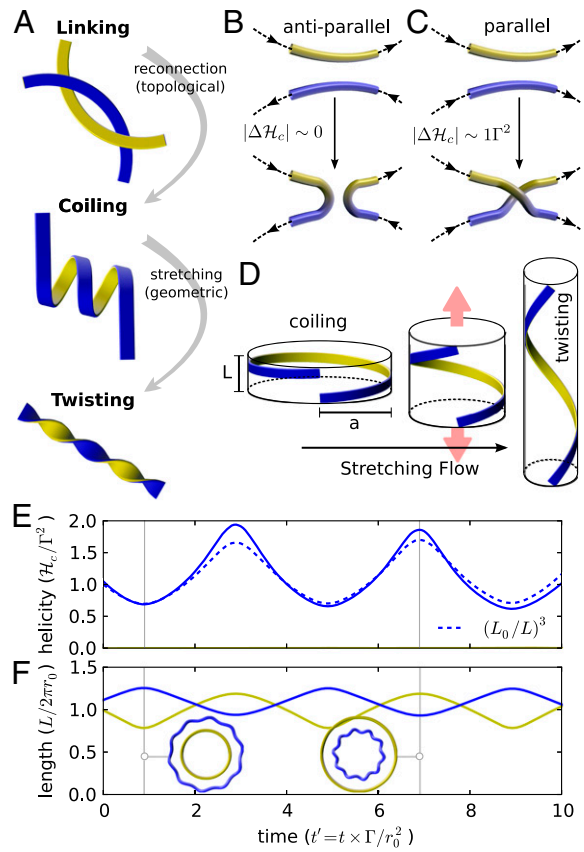

Fig. 6. (*A*) Illustrations of mechanisms for storing helicity on different spatial scales; in each case, the helicity of the depicted region is the same, $\mathcal{H}_c=2\Gamma^2$. Although linking is global in nature, both coiling and twisting are local—they produce linking between different subsections of the vortex tube, or in this case different edges of the illustrated ribbon. (*B* and *C*) Diagrams of reconnection events in locally antiparallel or parallel orientations. The antiparallel reconnection does not change helicity because it does not introduce a new "crossing" of the projected tubes, unlike the parallel reconnection. This antiparallel configuration tends to form spontaneously for topologically nontrivial vortices, even in the absence of viscosity, in which case helicity is efficiently converted from global linking to local coiling. (*D*) Coiling can be converted to twisting by stretching helical regions of the vortex; this mechanism conserves total helicity because it does not change the topology, but results in an apparent change of helicity when twist cannot be resolved. (*E* and *F*) The helicity (*E*) and length (*F*) as a function of time for a simulated geometrical evolution of a circular vortex ring (yellow) leap-frogging a vortex ring with a helix superimposed (blue).

Center-Line Helicity). If the flow is a uniform, volume-conserving strain, the number of turns is conserved and $a \propto L^{-1/2}$, resulting in $\mathcal{H}_c/\Gamma^2 = Wr \propto L^{-3}$. This simplistic model qualitatively captures the center-line helicity of the leap-frogging helix of Fig. 6*E*, indicating that the center-line helicity changes primarily because the helical ring is being stretched and compressed. In general, we expect geometric deformations of the vortex—including stretching—should result in continuous changes of the center-line helicity.

Does this imply helicity is not conserved even when the topology is constant? As discussed in the introduction, helicity can also be stored in twist of the vortex bundle, which is neglected in the center-line helicity. As a method for keeping track of the vortex bundle orientation, consider it is a ribbon. If we imagine wrapping this ribbon around a cylinder N times, we expect the linking between the edges of the ribbon to remain constant even if the cylinder changes shape (Fig. 6*D*). In this case, the total helicity is constant: $\mathcal{H}/\Gamma^2 = N = Wr_{\text{helix}} + Tw$ [this is a restatement of the Călugăreanu–White–Fuller theorem (7, 38)]. As the writhe contribution varies dramatically as the vortex is stretched, we conclude that twist must be created in the vortex core to compensate.

We expect similar conversion of writhe to twist is happening for stretching knots and links, although the nonuniform stretching present there produces a rich structure across scales, as seen in our helistograms (Fig. 4). For experimental vortices, the compensating twist should be present, but we are not able to directly resolve it; doing so is a challenging goal for future investigations. As previously noted, however, this twist should be dissipated relatively rapidly by viscosity if the core is small compared with the overall vortex dimensions. In the case of GPE-simulated vortices, the helicity smoothly varies before the reconnections—when rapid stretching is present—and because there is no method for storing twist it is simply lost. However, after the reconnections, the length and helicity stabilize, despite the fact that the vortices have large oscillating coils. (The smallest vortices show a slow decay of helicity after reconnection because short wavelength coils, $\lambda \sim \xi$, are radiated away as sound waves in the GPE.)

Geometric and Topological Mechanisms for Helicity Conservation. Our results show that helicity can be conserved in real fluids even when vortex topology is not, and that helicity may not be conserved even when tube topology is invariant. Vortex reconnections do not simply dissipate helicity, but rather mediate a flow from knotting and linking to coiling, typically from large scales to smaller scales (Fig. 6). The efficient conversion of helicity through a reconnection is due to the antiparallel vortex configuration (Fig. 6*B*) that forms naturally in our reconnecting vortices. Deformation of vortices may also convert coiling into twist on even smaller scales, where it may ultimately be dissipated. Interestingly, stretching plays a critical role in both topological and nontopological mechanisms for helicity transport, and is also observed to happen spontaneously for initial linked or knotted vortices. The mechanisms for helicity transport, from linking to coiling to twisting, all have a natural interpretation in terms of the field-line geometry, and as such these mechanisms may play an important role in any tangled physical field. Taken as a whole, our results suggest that helicity may yet be a fundamental conserved quantity, guiding the behavior of dissipative complex flows, from braided plasmas to turbulent fluids.

Note Added in Proof. In the concluding stages of this work we became aware of a parallel effort by Laing et al. (39), who independently identified the mechanism for conservation of link and writhe through reconnections and constructed a rigorous proof of the conservation of writhe of curves under the assumption of antiparallel reconnecting segments.

ACKNOWLEDGMENTS. We acknowledge the Materials Research and Engineering Centers (MRSEC) Shared Facilities at The University of Chicago for the use of their instruments. This work was supported by the National Science Foundation MRSEC Program at The University of Chicago (DMR-0820054). W.T.M.I. further acknowledges support from the A. P. Sloan Foundation through a Sloan fellowship, and the Packard Foundation through a Packard fellowship.

1. Moffatt HK (1969) Degree of knottedness of tangled vortex lines. *J Fluid Mech* 35(Pt 1):117–129.
2. Thomson W (1867) On vortex atoms. *Proc R Soc Edinburgh* VI:94–105.
3. Moffatt HK (2014) Helicity and singular structures in fluid dynamics. *Proc Natl Acad Sci USA* 111(10):3663–3670.
4. Ricca RL, Berger MA (1996) Topological ideas and fluid mechanics. *Phys Today* 49(12): 28–34.
5. Tkalec U, Ravnik M, Čopar S, Žumer S, Muševič I (2011) Reconfigurable knots and links in chiral nematic colloids. *Science* 333(6038):62–65.
6. Martinez A, et al. (2014) Mutually tangled colloidal knots and induced defect loops in nematic fields. *Nat Mater* 13(3):258–263.
7. Dennis MR, King RP, Jack B, O'Holleran K, Padgett M (2010) Isolated optical vortex knots. *Nat Phys* 6(1):118–121.
8. Kedia H, Bialynicki-Birula I, Peralta-Salas D, Irvine WTM (2013) Tying knots in light fields. *Phys Rev Lett* 111(15):150404.
9. Han D, Pal S, Liu Y, Yan H (2010) Folding and cutting DNA into reconfigurable topological nanostructures. *Nat Nanotechnol* 5(10):712–717.
10. Chichak KS, et al. (2004) Molecular borromean rings. *Science* 304(5675):1308–1312.
11. Sumners D (1995) Lifting the curtain: Using topology to probe the hidden action of enzymes. *Not Am Math Soc* 42(5):528–537.
12. Vachaspati T, Field GB (1994) Electroweak string configurations with baryon number. *Phys Rev Lett* 73(3):373–376.
13. Bekenstein JD (1992) Conservation law for linked cosmic string loops. *Phys Lett B* 282(1-2): 44–49.
14. Faddeev L, Niemi A (1997) Stable knot-like structures in classical field theory. *Nature* 387(6628):58–61.
15. Bewley GP, Paoletti MS, Sreenivasan KR, Lathrop DP (2008) Characterization of reconnecting vortices in superfluid helium. *Proc Natl Acad Sci USA* 105(37):13707–13710.
16. Cirtain JW, et al. (2013) Energy release in the solar corona from spatially resolved magnetic braids. *Nature* 493(7433):501–503.
17. Kimura Y, Moffatt HK (2014) Reconnection of skewed vortices. *J Fluid Mech* 751: 329–345.
18. Kida S, Takaoka M (1988) Reconnection of vortex tubes. *Fluid Dyn Res* 3:257–261.
19. Kleckner D, Irvine WTM (2013) Creation and dynamics of knotted vortices. *Nat Phys* 9(4):253–258.
20. Pitaevskii LP, Stringari S (2003) *Bose-Einstein Condensation* (Clarendon, Oxford).
21. Moreau JJ (1961) Constantes dun îlot tourbillonnaire en uide parfait barotrope. *C R Acad Sci Paris* 252:2810–2812.
22. Berger MA, Field GB (1984) The topological properties of magnetic helicity. *J Fluid Mech* 147:133–148.
23. Arnold VI (1986) The asymptotic Hopf invariant and its applications. *Selecta Math Sov* 5(4):327–375.
24. Eberly D (1996) *Ridges in Image and Data Analysis* (Kluwer Academic, Dordrecht, The Netherlands).
25. Kindlmann GL, San José Estépar R, Smith SM, Westin C-F (2009) Sampling and visualizing creases with scale-space particles. *IEEE Trans Vis Comput Graph* 15(6):1415–1424.
26. Sethian JA (1996) A fast marching level set method for monotonically advancing fronts. *Proc Natl Acad Sci USA* 93(4):1591–1595.
27. Proment D, Onorato M, Barenghi CF (2012) Vortex knots in a Bose-Einstein condensate. *Phys Rev E Stat Nonlin Soft Matter Phys* 85(3 Pt 2):036306.
28. Berloff NG (2004) Padé approximations of solitary wave solutions of the Gross-Pitaevskii equation. *J Phys Math Gen* 37(5):1617–1632.
29. Salman H (2013) Breathers on quantized superfluid vortices. *Phys Rev Lett* 111(16):165301.
30. Brissaud A, Frisch U, Leorat J, Lesieur M, Mazure A (1973) Helicity cascades in fully developed isotropic turbulence. *Phys Fluids* 16(8):1366–1367.
31. Pfister H, Gekelman W (1991) Demonstration of helicity conservation during magnetic reconnection using Christmas ribbons. *Am J Phys* 59(5):497–502.
32. Lau Y, Finn J (1996) Magnetic reconnection and the topology of interacting twisted flux tubes. *Phys Plasmas* 3(11):3983–3997.
33. Onsager L (1949) Statistical hydrodynamics. *Nuovo Cim* 6(2):249.
34. Feynman R (1955) Application of quantum mechanics to liquid helium. *Progress in Low Temperature Physics*, ed Gorter CJ (North-Holland, Amsterdam), Vol 1, pp 17–53.
35. Kerr RM (2011) Vortex stretching as a mechanism for quantum kinetic energy decay. *Phys Rev Lett* 106(22):224501.
36. Donzis Da, et al. (2013) Vorticity moments in four numerical simulations of the 3D Navier-Stokes equations. *J Fluid Mech* 732:316–331.
37. Paoletti MS, Fisher ME, Sreenivasan KR, Lathrop DP (2008) Velocity statistics distinguish quantum turbulence from classical turbulence. *Phys Rev Lett* 101(15):154501.
38. Moffatt H, Ricca R (1992) Helicity and the Calugareanu invariant. *Proc R Soc Math Phys Eng Sci* 439(1906):411–429.
39. Laing CE, Ricca RL, Sumners DWL (2014) Conservation of writhe helicity under antiparallel reconnection. arXiv:1410.3588v1.

Supporting Information

Scheeler et al. 10.1073/pnas.1407232111

SI Text

Definition of the Center-Line Helicity

In defining the "center-line helicity," we are forced to adopt a convention for the implied contribution of the twist component of the total helicity. Physically, this corresponds to making a choice for how the vortex bundle should be wrapped around the center-line when twist cannot be directly resolved (Fig. S1). Our definition corresponds to the total helicity of a bundle with particularly simple internal structure, so that the total twist component is zero, $Tw_i = 0$, resulting in the following:

$$\mathcal{H}_c \equiv \mathcal{H}_{\text{c, p.t.}} = \Gamma^2 \left(\sum_{i \neq j} \mathcal{L}_{ij} + \sum_i Wr_i \right). \quad \textbf{[S1]}$$

Such a result can be obtained by constructing a bundle using the "parallel transport" framing, defined as one for which the twist rate of the normal vector, $\hat{\boldsymbol{n}}$, is everywhere zero: $(\hat{\boldsymbol{n}} \times \partial_s \hat{\boldsymbol{n}}) \cdot d\boldsymbol{\ell} = 0$.

To illustrate the consequences of our convention, consider a helix defined by the following:

$$x = a \cos kz \quad \textbf{[S2]}$$

$$y = a \sin kz. \quad \textbf{[S3]}$$

For a section spanning $z = 0$ to $z = L$, the number of helical turns is $N = \frac{kL}{2\pi}$ and the writhe is as follows:

$$Wr = N(1 - \cos\theta), \quad \textbf{[S4]}$$

where the winding angle is $\theta = \tan^{-1} ka$. In the limit of small winding angle ($\theta \to 0$), the resulting helicity is then given by the following:

$$\mathcal{H}_{\text{c, p.t.}} = \Gamma^2 Wr \quad \textbf{[S5]}$$

$$\sim \Gamma^2 \frac{N\theta^2}{2}. \quad \textbf{[S6]}$$

This has the important property that helicity goes smoothly to zero as the helix is flattened into a straight line. One apparent disadvantage of the parallel transport framing is that, in general, it does not close, meaning that an individual vortex filament does not reconnect with itself in a single trip around the bundle. We note, however, that this is expected for continuum fields; so long as a local twist rate can be defined, a noninteger total twist can be computed and corresponds to the mean linking of vortex filaments in the bundle (1).

One way to resolve the nonclosure of the bundle is to use a Frenet–Serret basis (in other words, $\hat{\boldsymbol{n}}$ is the Frenet–Serret normal vector). In this case, the twist and helicity are given by the following:

$$Tw_{\text{f.s.}} = \frac{1}{2\pi} \int ds\ \tau = N \cos\theta \quad \textbf{[S7]}$$

$$\mathcal{H}_{\text{c, f.s.}} = \Gamma^2 \left(Wr + Tw_{\text{f.s.}} \right) = \Gamma^2 N. \quad \textbf{[S8]}$$

Note that this result always gives an integer ($n\Gamma^2$) helicity, which is independent of the winding angle. Plotting the bundle resulting from such a framing reveals the source of this extra helicity: the vortex filaments become significantly twisted as the winding angle is reduced (Fig. S1, left side). In fact, integer helicity always result for framings in which all filaments close with themselves, as they produce a uniform, integer filament linking. Furthermore, it follows that the helicity computed for such a bundle will change discontinuously under smooth deformations, as it is confined to integer values. This is especially problematic when computing the helicity for experimental data: even infinitesimal spirals will appear to have high helicity content, and so this convention produces wildly fluctuating center-line helicity. [In the context of the Frenet–Serret framing, this can also be viewed as due to the creation of inflection points, which cause the torsion to be undefined (2).]

In addition to its ease of computation, the center-line helicity for a parallel transport bundle has one other important property: it corresponds to the configuration that naturally results from viscous dissipation of the vortex core (as derived in the next section for a straight center-line). Moreover, our experimental results indicate that it is continuous through a vortex reconnection, suggesting it is the natural and relevant definition for helicity conservation.

Helicity Dissipation for a Twisted Core

Consider a straight center-line, uniformly twisted core vortex with profile:

$$\boldsymbol{\omega} = \Omega(r) \left(\hat{z} + r\tau\hat{\phi} \right), \quad \textbf{[S9]}$$

where $\Omega(r)$ is the scalar core profile and τ is the twist rate. The helicity dissipation rate is given by the following (3):

$$\partial_t \mathcal{H} = -2\nu \int \boldsymbol{\omega} \cdot (\nabla \times \boldsymbol{\omega})\ dV = -4\nu\tau \int \Omega^2(r) dA\, dz, \quad \textbf{[S10]}$$

which can be rewritten as a relative decay rate:

$$\partial_t \mathcal{H} = -\mathcal{H} \frac{8\pi\nu}{A_{eff}}, \quad \textbf{[S11]}$$

where A_{eff} is an effective core area given by the following:

$$A_{eff} = \frac{\left(\int \Omega(r) dA \right)^2}{\int \Omega^2(r) dA}. \quad \textbf{[S12]}$$

Equivalently, we note that this is equivalent to a dissipation of the total twist: $\partial_t Tw = -Tw \frac{8\pi\nu}{A_{eff}}$, where the total twist is given by $Tw = \int \tau ds$. For experimental vortices in a viscous fluid, the core size is expected to grow like $r \sim \sqrt{4\nu t}$, or ~2 mm for our experiments (for water, $\nu = 1.0\ \text{mm}^2 \cdot \text{s}^{-1}$ and the typical experimental timescale is $t \sim 1$ s, which is roughly the time at which the reconnection start). The resulting dissipation rate is as follows: $\partial_t Tw / Tw \sim 5\ \text{s}^{-1}$.

Experimental Vortex Generation

The experiments were carried out using the vortex generation and imaging techniques described in ref. 4. Vortices are generated using shaped hydrofoils generated by a 3D printer. These hydrofoils are attached to a frame, which is then rapidly accelerated using a short, open pneumatic cylinder driven by a quick-release

valve, where typical accelerations are on the order of $a = 285$ m/s^2, reaching speeds of $U \sim 2$ m/s. The hydrofoils used for the data shown in the main text have a chord of $Ch = 22.5$ mm, a leading edge thickness of $t_1 = 3.75$ mm, a trailing edge thickness of $t_2 = 0.225$ mm, and a bend of $\theta = 15°$. Images of the 3D models used to print each hydrofoil are reproduced in Fig. S2.

The trailing edge path (which is traced by the resulting vortices) had an r.m.s. radius of $\bar{r} = 69.3$ mm in the case of the trefoil knot and an r.m.s. radius of $\bar{r} = 75.5$ mm in the case of the linked rings. Hydrofoils (and vortices) have also been generated at smaller scales and are observed to have qualitatively similar dynamics. A volumetric image of the vortex core is obtained with a laser-scanning tomography apparatus (the obtained volumes have a size of 384^3 voxels with an adjustable resolution of 0.6 mm/voxel). The effects of perspective in the imaging apparatus are corrected for in the resulting data. The circulation of the vortices is estimated using the formula for the circulation around a thin flat plate in inviscid flow (5):

$$\Gamma = \pi \; U \; Ch \sin\alpha, \qquad \textbf{[S13]}$$

where $\alpha \approx \theta/2$ is the effective angle of attack. The speed of the hydrofoil is directly measured using an encoder attached to the hydrofoil acceleration frame. The circulation obtained from this estimate is consistent with the forward speed of simple vortex rings and the stretching rate observed for knotted vortices.

Experimental Vortex Shape Reconstruction

To reconstruct the shape of the vortices from experimental volumetric data, we have adapted methods from biomedical image analysis. Due to the nature of the raw data, some apparent gaps along the vortex path may arise from nonuniform bubble density. Previously, manual identification of vortices was used, along with automated line tracing (4). As an improvement, we have developed a two-step process for numerically identifying vortices before joining them together into a complete path.

Vortices appear as one-dimensional ridge lines in the 3D image: the locus of points for which image intensity is maximized relative to motion along the minor and medium eigenvectors of the image Hessian (6). For the detection and spatial localization of vortices, we adapt a method of particle-based ridge sampling (7). Image identification "particles" move within the image domain, subject to forces from other particles, while constrained to stay within ridge lines. These particles are subject to a synthetic radial potential function that monotonically decreases away from $r = 0$ but with a slight attractive potential well at tunable position, producing approximately equidistant spacing. The point locations are iteratively updated to minimize the total energy of the system. Points are periodically added to ensure complete coverage of detected ridge features and deleted where the feature fades to noise. For each energy-minimizing iteration, the points are constrained to ridges with Newton optimization using the gradient and Hessian of the continuous image, as reconstructed by convolution with the C^2 cubic B-spline.

Once particles have converged, the recovered vortex segments are joined via fast marching (8).

Calculation of Linking and Writhe

Linking and writhe are computed by projecting the 3D paths into a plane and counting signed crossings between line segments. To protect against numerical errors, which may be especially problematic with the noisy experimental data, three random orientations are checked for consistency, and more orientations are computed if the results do not agree. To compute the noninteger portion of the writhe, an additional term is added to account for the twist of the implied framing (9). A black-board framing (i.e., a framing chosen to always be exactly perpendicular to the projection direction) is used instead of the traditional Frenet–Serret framing; this was found to produce more accurate results in the presence of noise, as confirmed by comparing the results to the average summed crossing number over random projections.

Theory of Helicity Conservation Through a Reconnection

As described in the main text, the conservation of helicity in reconnecting vortices is due to the reconnection events happening across regions where the vortex path is antiparallel. Typically, linking is described in terms of planar knot diagrams; however, in this case, it does not produce an intuitive description of the observed mechanism. For example, vortex reconnections are conventionally depicted as taking place at crossings in a planar diagram (Fig. S3*A*), leading one to the incorrect conclusion that helicity must change by $|\Delta\mathcal{H}_c| = 1\Gamma^2$. (We note that, in all cases, the center-line helicity is given by the following: $\mathcal{H}_c/\Gamma^2 = \sum \mathcal{L}_{ij} + \sum Wr_i = N_+ - N_-$, where $N_\pm$ are the number of signed crossings, averaged over all projections. For nearly planar shapes, all projections have the same number of crossings.) We can modify our diagram to add two-antiparallel extensions and place the reconnection in this region; in this case, we conclude the helicity is conserved (Fig. S3*B*). Although this geometry seems unintuitive in a plane, it forms naturally for fully 3D paths. This is particularly true for reconnecting vortices driven by stretching, which are expected to adopt an antiparallel configuration to conserve energy (4). In the event that the reconnection is not perfectly antiparallel, as is apparently the case for small GPE vortices, this conservation may be imperfect.

Helistogram Analysis

Helistograms for a given curve are constructed by smoothing the original path with a Blackmann windowed sinc kernel of increasingly larger cutoff wavelengths incremented by a small $d\lambda$. By taking the difference between the helicity $\mathcal{H}(\lambda)$ calculated for a path smoothed by λ and the helicity $\mathcal{H}(\lambda + d\lambda)$ of the slightly more smoothed path, we can compute the helicity stored on the scale of λ. This progressive smoothing process can be seen in Movie S1, which shows the path corresponding to each cutoff wavelength.

For a helically wound ring, the locations of the peaks on a helistogram correspond to the helical wavelength L/n of the path, where L is the total length of the path and n is the winding number. A collection of helically wound rings with different values of L/n along with their corresponding helistograms are shown in Movie S2. Note that, as the helical wavelength of the structures increases, the helicity should decrease in magnitude and shift to larger length scales, both of which are captured by the shrinking and translation of the single peak in the helistogram. Helistograms can also be constructed for GPE data, as shown in Fig. S4; the results are qualitatively similar to experimental data for the same initial shape, although all three reconnections happen simultaneously.

Gross–Pitaevskii Equation

Simulations of the Gross–Pitaevskii equation (GPE) were carried out using the same parameters as in ref. 10, where the GPE is considered in a dedimensionalized form:

$$2i\partial_t\Psi + \nabla^2\Psi - |\Psi|^2\Psi = 0, \qquad \textbf{[S14]}$$

where the circulation in these units is $\Gamma = 2\pi$, the healing length is $\xi = 1$, and we set a far-field density of $\rho_\infty = |\Psi_\infty|^2 = 1$. The simulations used a grid size of $\Delta x = \xi/2$ and time step $\Delta t = 0.02$, using periodic boundary conditions. The initial phase field was constructed by brute-force integration of the velocity field generated by the vortices (obtained from the Biot–Savart law), making use of the following relation:

$$\phi_{x_1} - \phi_{x_0} = \int_{x_0}^{x_1} \boldsymbol{v} \cdot d\boldsymbol{\ell}, \qquad \textbf{[S15]}$$

where the periodicity is ensured by calculating the flow field for periodically copied versions of the desired vortex. (In practice, we use a $5 \times 5 \times 5$ cube of vortex copies, where the flow field is calculated in the central volume; this number was chosen empirically to produce smooth boundaries that do not generate sound waves when the simulation begins.) A similar integration method has recently been used for GPE simulations in other contexts (11). To create a phase volume, an arbitrary phase is assigned to one corner, which is then extended to a plane on one edge of the volume. Integrating from this plane then produces a phase volume. To ensure that the phase matches across periodic boundaries, a constant gradient is added. (This is equivalent to removing the uniform background flow produced by a periodic collection of vortex loops.)

The initial density field was calculated using a Padé approximant (12):

$$\rho(r) = \frac{\frac{11}{32} r^2 + \frac{11}{384} r^4}{1 + \frac{1}{3} r^2 + \frac{11}{384} r^4}, \qquad \textbf{[S16]}$$

where r was taken to be the distance to the closest vortex line. The vortex knot with r.m.s. radius $\bar{r} = 24\xi$ was simulated in a periodic cube with edge $a = 128\xi$ (256 grid points), and the simulation volume was scaled in proportion to the knots for other sizes. Weak density waves are observed to radiate from the vortex at the beginning of the simulation (due to the fact that the vortex curvature relaxes the core profile to a slightly different form than that given by the Padé approximant), resulting in a small reduction of the vortex length and energy from the initial condition. Vortex paths were obtained by tracing the phase defects in the simulated wave function. Time steps when the vortices begin to overlap, defined as when the vortex separation is less than $r_{min} < 2\xi$, are omitted from Fig. 4.

Biot–Savart Evolution of Thin Core Vortices

The Biot–Savart velocity of the vortex is calculated using an exact expression for the flow generated by nonadjacent segments (modeled as a polygonal path), and an explicit expression for the flow generated by the neighboring segments (treated as a circular arc going through the 3-point neighborhood). Time integration is performed using a fifth order Runge–Kutta scheme [Dormand–Prince (13)] with an adaptive time step so that the velocity error is kept below $\delta v < \sim 10^{-10}\Gamma/r_0$ (with segment length $\Delta\ell \sim 0.05$).

1. Arnold VI (1986) The asymptotic Hopf invariant and its applications. *Selecta Math Sov* 5(4):327–375.
2. Moffatt H, Ricca R (1992) Helicity and the Calugareanu invariant. *Proc R Soc Math Phys Eng Sci* 439(1906):411–429.
3. Moffatt HK (1969) Degree of knottedness of tangled vortex lines. *J Fluid Mech* 35(Pt 1):117–129.
4. Kleckner D, Irvine WTM (2013) Creation and dynamics of knotted vortices. *Nat Phys* 9(4):253–258.
5. Acheson DJ (1990) *Elementary Fluid Dynamics* (Clarendon, Oxford).
6. Eberly D (1996) *Ridges in Image and Data Analysis* (Kluwer Academic, Dordrecht, The Netherlands).
7. Kindlmann GL, San José Estépar R, Smith SM, Westin C-F (2009) Sampling and visualizing creases with scale-space particles. *IEEE Trans Vis Comput Graph* 15(6):1415–1424.
8. Sethian JA (1996) A fast marching level set method for monotonically advancing fronts. *Proc Natl Acad Sci USA* 93(4):1591–1595.
9. Klenin K, Langowski J (2000) Computation of writhe in modeling of supercoiled DNA. *Biopolymers* 54(5):307–317.
10. Proment D, Onorato M, Barenghi CF (2012) Vortex knots in a Bose-Einstein condensate. *Phys Rev E Stat Nonlin Soft Matter Phys* 85(3 Pt 2):036306.
11. Salman H (2013) Breathers on quantized superfluid vortices. *Phys Rev Lett* 111(16): 165301.
12. Berloff NG (2004) Padé approximations of solitary wave solutions of the Gross-Pitaevskii equation. *J Phys Math Gen* 37(5):1617–1632.
13. Dormand J, Prince P (1980) A family of embedded Runge-Kutta formulae. *J Comput Appl Math* 6(1):19–26.

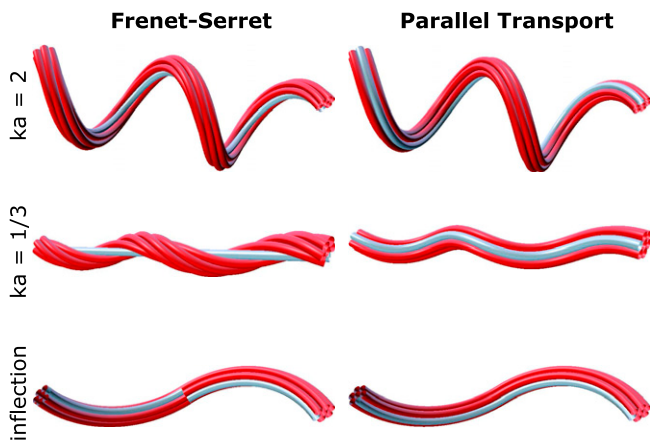

Fig. S1. An illustration of the vortex bundles produced for spiral-like center-lines using different framing methods. The left column shows bundles oriented with the Frenet–Serret normal vector, whereas the right uses a parallel transport (untwisted) framing. The first two rows are helices, whereas the third row shows an inflection point produced by merging two circular arcs.

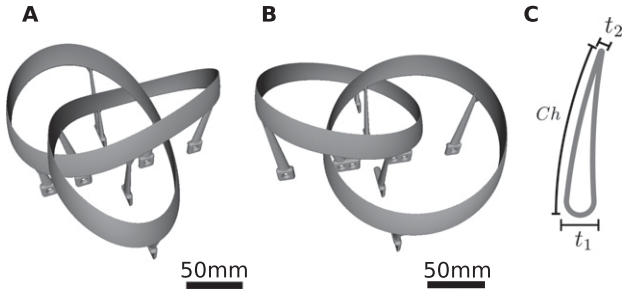

Fig. S2. (*A*) A 3D rendering of the trefoil knot hydrofoil used in experiment. (*B*) A 3D rendering of the link rings hydrofoil used in experiment. (*C*) The hydrofoil cross-section used in both the trefoil knot and linked rings with the following specifications: a chord of $Ch = 22.5$ mm, a leading edge thickness of $t_1 = 3.75$ mm, a trailing edge thickness of $t_2 = 0.225$ mm, and a bend of $\theta = 15°$.

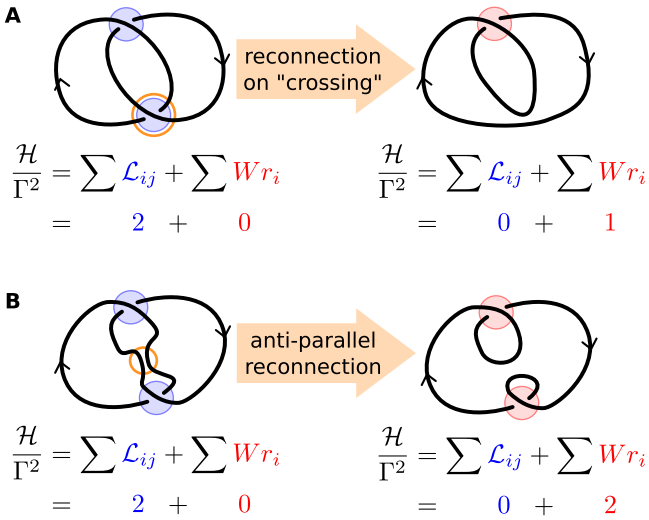

Fig. S3. (*A*) A diagram of a reconnection event occurring at a "crossing" for a nearly planar pair of linked rings. The helicity has an apparent change of $1\Gamma^2$ because an in-plane crossing is eliminated. (*B*) A reconnection event that occurs between antiparallel segments does not change the crossing number and so it conserves helicity.

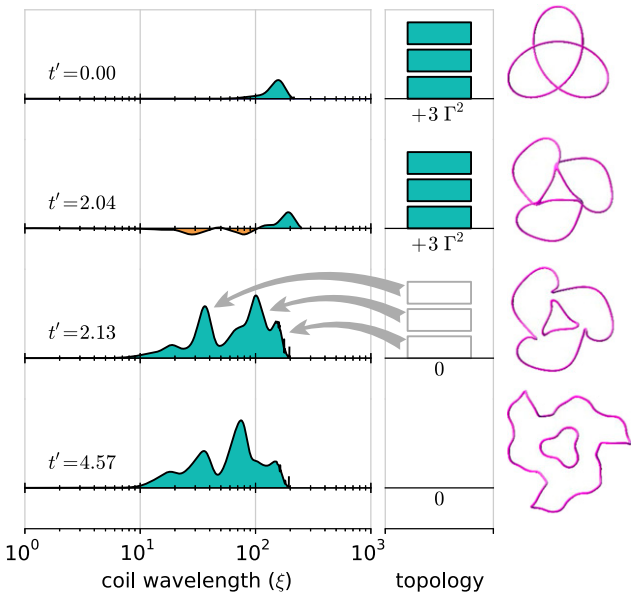

Fig. S4. A helistogram for a GPE trefoil knot with $\bar{r} = 36\xi$, shown along with renderings of the density iso-surfaces at the same simulation time. Unlike in the experiments, the perfect symmetry of the simulation causes all three reconnections to happen simultaneously, transferring nearly all of the helicity from knotting to coiling in a single event.

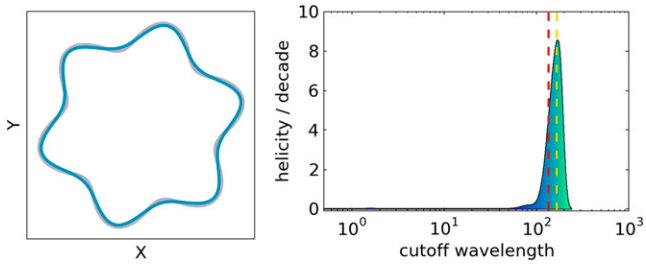

Movie S1. The construction of a helistogram for a helical ring with $n = 6$ windings. The smoothed path corresponding to each cutoff wavelength is shown (*Left*) along with the complete helistogram (*Right*). The cutoff of the current smoothing is indicated with the red dashed line; for cutoff values below the wavelength L/n (dashed gold line), the path is unaffected by the smoothing; however, once the cutoff value approaches L/n, the helix is rapidly smoothed down to a ring of zero helicity.

Movie S1

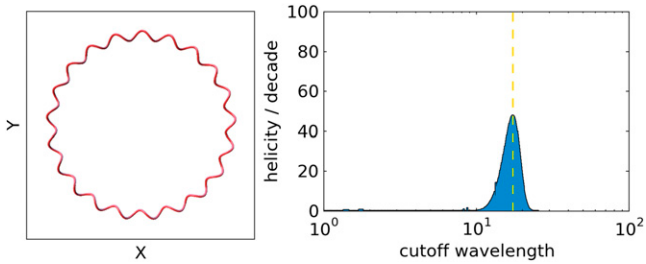

Movie S2. A video showing the helistograms (*Right*) for a collection of different helically wound rings (*Left*) with progressively smaller winding numbers, *n*, but with constant radii and helical amplitude. As the pitch of the helices increases, the helicity of the path becomes localized at progressively larger scales while diminishing in overall magnitude.

Movie S2

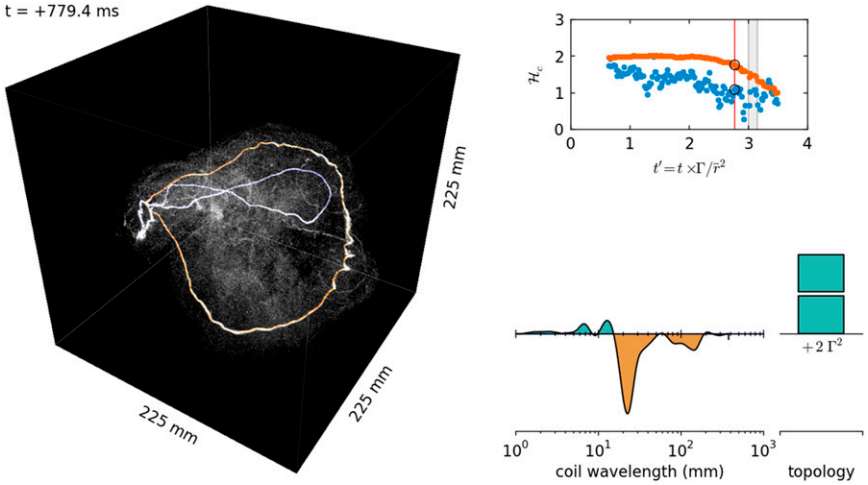

Movie S3. A volumetric image of a pair of linked vortices (*Left*), along with the total helicity (*Upper Right*) and helistogram (*Lower Right*) as a function of time. The initially linked vortices go through two reconnections to form a pair of unlinked rings, which results in the formation of large-scale helices with approximately the same amount of helicity as the initial linking. The volumetric data were recorded at 169.4 volumes per second, and is played back at 15 frames per second, except near the reconnection events where the playback is slowed to 3 frames per second. In frames for which the vortices could be successfully tracked, they are highlighted in blue and orange (corresponding to the first and second identified vortex loop).

Movie S3

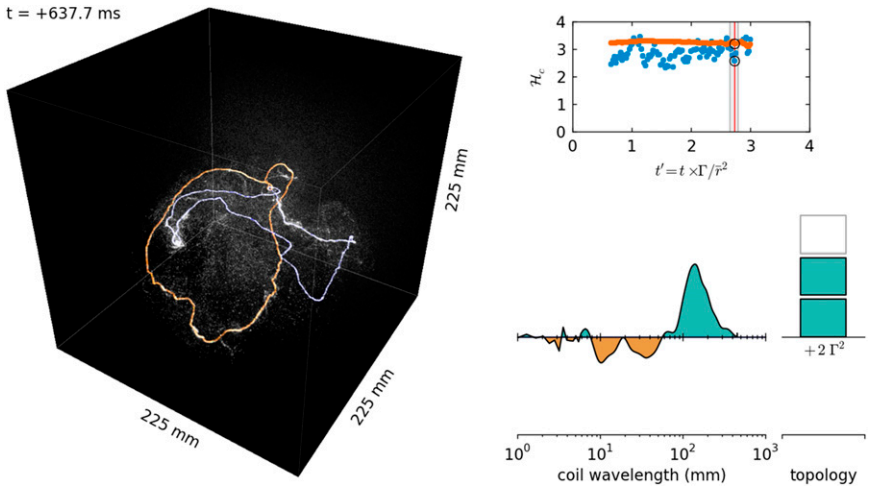

Movie S4. A volumetric image and helistogram for a vortex that is initially a trefoil knot, displayed as in Movie S3. The trefoil knot goes through three reconnections to become a pair of unlinked rings, although it is only possible to track it through the first two reconnections.

Movie S4

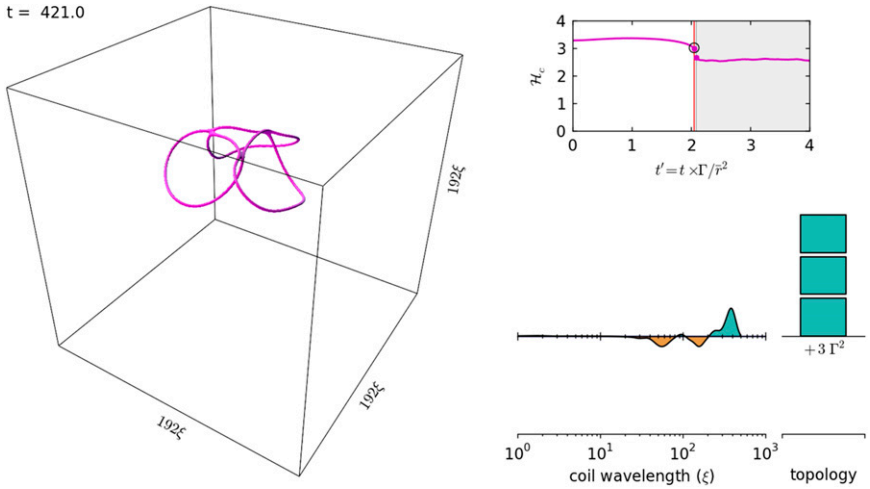

Movie S5. The density isosurface and helistogram for a Gross–Pitaevskii simulated trefoil vortex knot with mean radius $\bar{r} = 36\xi$. The final topology (two unlinked rings) is the same as the viscous fluid trefoil vortex knot, although all three reconnections happen simultaneously due to the perfect symmetry of the simulation.

Movie S5

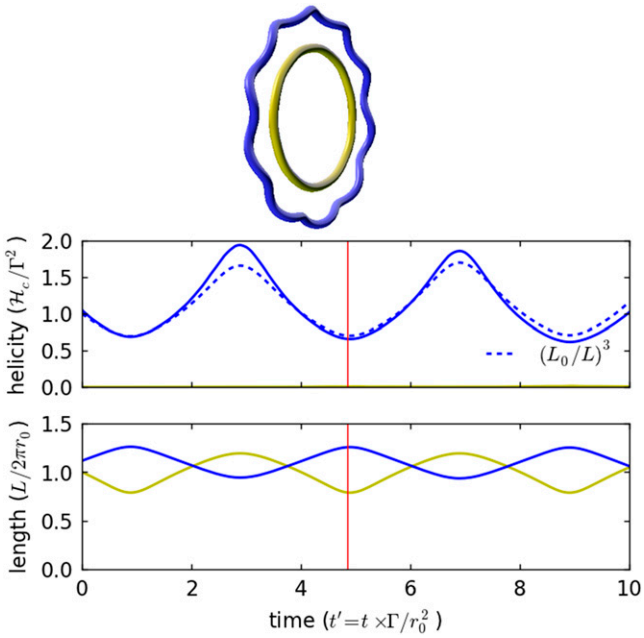

Movie S6. A Biot–Savart simulation of a helical vortex ring leap-frogging a perfectly circular ring. A rendering of the 3D vortex paths is shown, along with the helicity and length as a function of time. The stretching and compressing experienced by the helical ring causes its helicity to vary dramatically.

Movie S6